

## Atomic force microscopy bending tests of a suspended rod-shaped object: Accounting for object fixing conditions

Alexander Ankudinov <sup>1,\*</sup>, Mikhail Dunaevskiy,<sup>1</sup> Maksim Khalisov <sup>1,2</sup>, Ekaterina Khrapova,<sup>1</sup> and Andrei Krasilin <sup>1</sup>

<sup>1</sup>*Ioffe Institute, St. Petersburg 194021, Russia*

<sup>2</sup>*Pavlov Institute of Physiology, Russian Academy of Sciences, St. Petersburg 199034, Russia*



(Received 25 October 2022; accepted 9 February 2023; published 27 February 2023)

The technique of atomic force microscopy (AFM) bending tests of a suspended nano-object (scroll, tube, rod) makes it possible to calculate the Young's modulus of the material it is made of based on experimental data. However, the calculation results involve a large error due to uncertain conditions (console or bridge) of fixing the test object. One of the ways to reduce this error is based on the theoretical consideration of consoles or bridges as beams with one or two ends resting on Winkler elastic foundations. The beam bending problems have been solved in both cases using Krylov's functions. This has allowed for developing an approach to the analytical identification of fixing conditions and including them in the calculations. The application of the approach is illustrated by AFM measurements of the Young's modulus of  $\text{MgNi}_2\text{Si}_2\text{O}_5(\text{OH})_4$  nanoscrolls.

DOI: [10.1103/PhysRevE.107.025005](https://doi.org/10.1103/PhysRevE.107.025005)

### I. INTRODUCTION

Atomic force microscopy (AFM) [1] is designed to study surfaces using a nanometer-sharp probe. The probe is mounted on a cantilever, the deformation of which is measured to control the force of interaction with the sample [2]. To keep the probe sharp, the force is maintained at a level of  $\sim 1$  nN. By indenting the probe with this force into a soft material of the sample (Young's modulus  $E \sim 1$  GPa) and determining the sample deformation, it is possible to map changes in the value of  $E$  on its surface with nanoscale resolution [3].

The Young's modulus of a solid material ( $E \sim 100$  GPa) can be determined using the method of AFM bending tests of the suspended object [4]. Quasi-one-dimensional objects deposited from colloidal drops on substrates with grooves can form consoles or bridges over the grooves [5–7]. By AFM-aided measurement of the minimum stiffness of the suspended object,  $k_{\min}$ , one can calculate  $E$  using the theory of small deflections of rods [8].

The main error of this technique arises due to the unknown object fixing conditions [9–12]. For example, both clamped and supported beams (“CB” and “SB,” respectively) correspond to a bridge of a given minimum stiffness with the Young's moduli of the beams differing by a factor of 4,

$$\begin{aligned} E_{\text{CB}} &= \frac{k_{\min} l^3}{192I} = \frac{k_{\min} l^3}{3\pi d^4}, \\ E_{\text{SB}} &= \frac{k_{\min} l^3}{48I} = 4E_{\text{CB}}. \end{aligned} \quad (1)$$

The bridge is characterized by the span length  $l$  and the moment of inertia  $I$  ( $I = \pi d^4/64$  for a cylindrical rod of diameter  $d$ ).

It was proposed to reduce [9–11] and even completely eliminate [12–14] the fourfold uncertainty by matching the

measured bending of the object at the load point as a function of load position with the model. The paper [12] proposed a fitting curve that transforms from the CB to the SB case when varying the dimensionless parameter  $\lambda \in [0, \infty)$ . A continuous transition between the extremes gives a solution of the problem of a beam on ring springs whose angular stiffness depends on  $\lambda$  [Fig. 1(b)]. The value of  $\lambda$  with the best possible fit to the experiment determines a correction factor  $\Phi_1(\lambda) \in [1, 4]$  and the corrected Young's modulus  $E_{\text{corr}} = \Phi_1 E_{\text{CB}}$  [12–14].

The paper [15] considered the problems of a console on ring spring and a beam on Winkler elastic foundation with a suspended console (models 1 and 2 in Fig. 1 and Table I). The console fixing conditions affect the shape of the fitting curves  $\zeta_1$  and  $\zeta_2$  through the values of the parameters  $\lambda, \beta_l \in [0, \infty)$ , respectively. The corrected Young's modulus of the console is calculated as  $E_{\text{corr}} = \Phi_1(\lambda)E_0$  or  $E_{\text{corr}} = \Phi_2(\beta_l)E_0$ . In contrast to model 1 for a bridge, both correction factors for the console can be arbitrarily large,  $\Phi_1, \Phi_2 \in [1, \infty)$ . The value of  $E_0$  is calculated according to model 0,

$$E_0 = \frac{k_{\min} l^3}{3I} = \frac{64k_{\min} l^3}{3\pi d^4}, \quad (2)$$

for a cylindrical console of length  $l$  and diameter  $d$ . In contrast to model 1, applying model 2 to the console produced a result comparable to the Young's modulus for bridges [15].

In the general case, both the object and the substrate are deformed during testing. Taking this into account, the problem of a beam on the Winkler elastic foundation [16] was considered in [7]. However, the authors of [7] did not provide compact formulas for the console or bridge bending (or the stiffness, inversely proportional to it) at the load point as functions of the load position. This is done in the present paper. Within the framework of the considered AFM method, the present result and the paper [15] provide a comprehensive set of tools to analytically identify and account for the fixing conditions of the suspended object, as discussed below.

\*alexander.ankudinov@mail.ioffe.ru

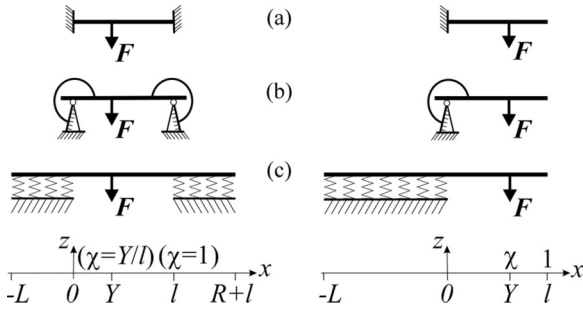


FIG. 1. Model 0: console or bridge with clamped ends (a). Model 1: console or bridge mounted on ring springs (the torque  $EIz''$  created by such a spring is proportional to the beam deflection angle  $z'$ ) (b). Model 2: console or bridge on Winkler elastic foundation with Winklers coefficient  $k_W$  and lengths  $L$  and  $R$  (c). The origin is located on the left support edge, the console and bridge lengths are  $l$ , and the force  $F$  is applied at  $x = Y$ .

## II. MODELING

Figure 1 shows six model schemes with three options for fixing the endpoints of the bridges and consoles on the supports. For each scheme, the derivation of the formula for the bending profile of the entire suspended object loaded at the point  $x = Y$  can be found in [8,12,15] and in the Appendix to this paper. In the AFM bending tests described here, it is not this profile that is measured but the dependence of the bending  $z(Y)$  on the load application position. The fitting curves for experimental data are functions of the normalized bending amplitude  $\zeta_i = z(\chi)/z_{\text{MAX}}$  with dimensionless variable  $\chi = Y/l$  ( $l$  is the length of the suspended part of the object; see Table I).

In model 1 with ring springs as supports (see also [12,15]), both dependences  $\zeta_i$  are related to the solution of the equation  $z^{IV} = 0$ . For a console, the solution satisfies the boundary conditions on the left support and at the load point,  $z(0)=0$ ,  $z''(0)=4z'(0)/(\lambda l)$  and  $z''(Y) = 0$ ,  $z'''(Y) = -F/EI$ . For a

bridge, the boundary conditions are added to the right support,  $z(l) = 0$  and  $z''(l) = -4z'(l)/(\lambda l)$ .

The exact solution for a console in model 2 was obtained in [15] using Krylov's functions [17]. A more complicated case of a bridge in the same model is considered in the Appendix to this paper. A relatively compact solution is obtained only in the asymptotic approximation. The asymptotes of the Krylov functions can be applied under the conditions  $L\sqrt[4]{k_W/4EI}$  and  $R\sqrt[4]{k_W/4EI} \gg 1$ , where  $k_W$  relates the linear force and the deflection of the Winkler elastic foundation, and  $L$  and  $R$  are support lengths [see Fig. 1(c)]. Let us consider a rigid cylinder of length  $L$  (a nanoscroll) indented by a force  $F_i$  into the foundation (support) to depth  $z_i$ . Then for the force per unit length, we can write [18]  $F_i/L \approx [\pi E_S/4(1 - \nu_S^2)]z_i$ , where  $E_S$  and  $\nu_S$  are Young's modulus and Poisson's ratio of the foundation. Based on this, we have  $k_W \approx E_S$ . If for  $l$  we take the moment of inertia of a cylinder with diameter  $d$ , the conditions are transformed to the form  $Ld^{-1}(E_S/E)^{1/4}$ ,  $Rd^{-1}(E_S/E)^{1/4} \gg 1$ . The support length is usually much greater than the object transverse dimensions, and the Young's moduli of the object and the support are comparable in value; therefore, these conditions are met in AFM bending tests. The formulas for  $\zeta_2$  and  $\Phi_2$  given in Table I for console and bridge are obtained in asymptotic approximation.

## III. AFM MEASUREMENTS

$\text{MgNi}_2\text{Si}_2\text{O}_5(\text{OH})_4$  nanoscrolls grown by hydrothermal synthesis were studied in [15,19]. Hydrosilicates with the structures of chrysotile, pectorate, and halloysite [20] fold into long tubes and scrolls with outer and inner diameters of 20–200 and 4–30 nm, respectively. Such shapes compensate for the mechanical stresses of the mismatched crystal lattices of the sublayers of the composite hydrosilicate bilayer of metal-oxygen and silicon-oxygen [21]. Since hydrosilicate nanoscrolls are promising for applications as adsorbents and capsules [22–24], catalysts [25–29], and reinforcing additives of composite materials [30–33], information on the Young's moduli of individual nanoscrolls is required.

TABLE I. Fitting curves and correction factors of three models for determining Young's modulus based on AFM bending test data of suspended objects. The parameters  $\lambda \in [0, \infty)$  and  $\beta_i \in [0, \infty)$  as well as the variable  $\chi \in [0, 1]$  are dimensionless. For console,  $E_{\text{corr}} = \Phi_i E_0$  and for bridge,  $E_{\text{corr}} = \Phi_i E_{\text{CB}}$ .

Model number $i$ , object type	$\zeta_i$ , fitting curve	$\Phi_i$ , correction factor
0: console	$\chi^3$	1
0: bridge	$64(\chi - \chi^2)^3$	1
1: console	$\frac{3\lambda\chi^2 + 4\chi^3}{3\lambda + 4}$	$1 + \frac{3\lambda}{4}$
1: bridge	$32 \frac{3\lambda(\lambda + 1)(\chi - \chi^2)^2 + 2(\lambda + 2)(\chi - \chi^2)^3}{(2\lambda + 1)(3\lambda + 2)}$	$1 + \frac{3\lambda}{\lambda + 2}$
2: console	$\frac{3 + 6\beta_i\chi}{3 + 6\beta_i + 6\beta_i^2 + 2\beta_i^3} + \frac{6\beta_i^2\chi^2 + 2\beta_i^3\chi^3}{3 + 6\beta_i + 6\beta_i^2 + 2\beta_i^3}$	$1 + \frac{3 + 6\beta_i + 6\beta_i^2}{2\beta_i^3}$
2: bridge	$32 \frac{3(6 + 12\beta_i + 12\beta_i^2 + 6\beta_i^3 + \beta_i^4) + 6(3 + 4\beta_i + \beta_i^2)\beta_i^3(\chi - \chi^2)}{(2 + \beta_i)(12 + 12\beta_i + 6\beta_i^2 + \beta_i^3)(24 + 12\beta_i + 6\beta_i^2 + \beta_i^3)}$ $+ 32 \frac{6(1 + 3\beta_i + \beta_i^2)\beta_i^4(\chi - \chi^2)^2 + 2(2 + \beta_i)\beta_i^6(\chi - \chi^2)^3}{(2 + \beta_i)(12 + 12\beta_i + 6\beta_i^2 + \beta_i^3)(24 + 12\beta_i + 6\beta_i^2 + \beta_i^3)}$	$1 + \frac{24 + 12\beta_i + 6\beta_i^2}{\beta_i^3}$

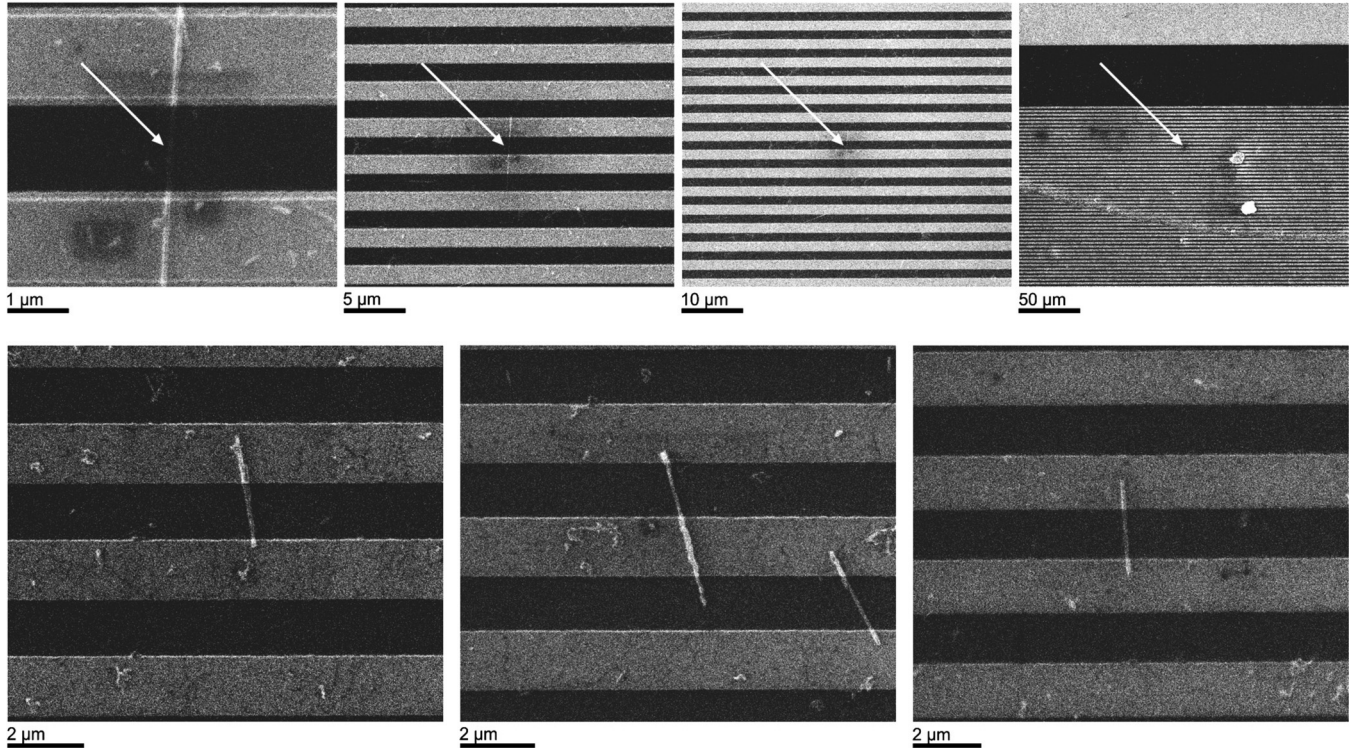


FIG. 2. SEM images of the TGZ2 calibration grating with hydrosilicate nanoscrolls. The top row is a typical set of images used to facilitate the optical positioning of an AFM probe near a suspended nanoscroll (the arrows indicate the location of the nanoscroll). The bottom row shows images of suspended nanoscrolls.

Nanoscrolls were deposited on a TGZ2 calibration grating (NT-MDT SI, Russia) with a period of  $3 \mu\text{m}$  and a groove depth of  $110 \text{ nm}$ . The bridges or consoles formed above the grating grooves were determined (see Fig. 2) using a Quanta 200 scanning electron microscope (SEM; FEI, USA). This considerably accelerated the subsequent search for such nanoscrolls with a Z16 APO optical microscope (Leica, Germany) combined with an atomic force microscope BioScope Catalyst (Bruker, USA). AFM bending tests were carried out in the PeakForce quantitative nanomechanics (QNM) mode with automatic analysis of the force curves recorded when the probe contacts the surface. We used FMG01 cantilevers (NT-MDT SI, Russia), with the value of the spring constant refined by the thermal-noise based method [34]. Scanning was carried out with a peak force leading to a nanoscroll bending of  $\sim 10 \text{ nm}$ . AFM signals of height, deformation, and peak force errors were recorded [14,15]. They were used to correct the deformation signal taking into account the contribution of methodological factors, including slipping of the AFM probe on inclined sections of the sample [14,35]. Two deformation profiles along the nanoscroll were analyzed with different start and end positions after correction. One profile corresponded to the suspended part of the nanoscroll according to AFM topography, and the length of the other one was determined by the nonzero deformation domain. Young's modulus was calculated based on the best-fit profile with  $\zeta_i$ , Table I. The GWYDDION 2.55 software [36] was used to process the AFM data.

Figure 3 shows the AFM bending test data for two suspended nanoscrolls. The following parameters were de-

termined for bridge and console, respectively:  $l = 1530 \text{ nm}$ ,  $385 \text{ nm}$ ;  $d = 49 \text{ nm}$ ,  $51 \text{ nm}$ ;  $k_{\min} = 2.4 \text{ N/m}$ ,  $1.3 \text{ N/m}$ ;  $E_{\text{CB}} = 156 \text{ GPa}$ ,  $E_0 = 75 \text{ GPa}$  (model 0);  $\lambda = 0.05$ ,  $67$  and  $E_{\text{corr}} = 167 \text{ GPa}$ ,  $3.83 \text{ TPa}$  (model 1);  $\beta_l = 74$ ,  $2.4$  and  $E_{\text{corr}} = 169 \text{ GPa}$ ,  $216 \text{ GPa}$  (model 2). In this example, the values of  $E_{\text{corr}}$  for console and bridge in model 1 differ by 23 times and for model 2, by 28%.

#### IV. RESULTS AND DISCUSSION

Let us consider the results of AFM bending tests for 31 bridges and 18 consoles. In the phase plane in Fig. 4(a), suspended objects correspond to points. The abscissa of each point is given by the dimensional parameter  $d^4 l^{-3}$  and the ordinate, by the value of  $k_{\min}$  for bridge or  $64k_{\min}$  for console. In the log-log data scale, the  $E$  contours are straight lines of unit slope. The bridge is larger than the grating groove width ( $\approx 1.5 \mu\text{m}$ ) and the console, on average, is almost an order of magnitude shorter than the bridge. Therefore, in the phase plane, the data points corresponding to the bridges are mainly on the lower left, and those of the consoles are on the upper right. According to model 0, the Young's modulus of consoles is 30% less than that of bridges (see Table II). Figure 4(a) illustrates this clearly, as the cluster of points of all tested objects is elongated at a flatter angle than the isolines of  $E$ .

After applying models 1 and 2, the corrected data points of the tested objects changed their position on the phase plane [see Figs. 4(b) and 4(c)]. The cluster slope became steeper in both cases. According to model 1 applied to 13 consoles out of 18, the value of  $E$  turned out to be four times greater than

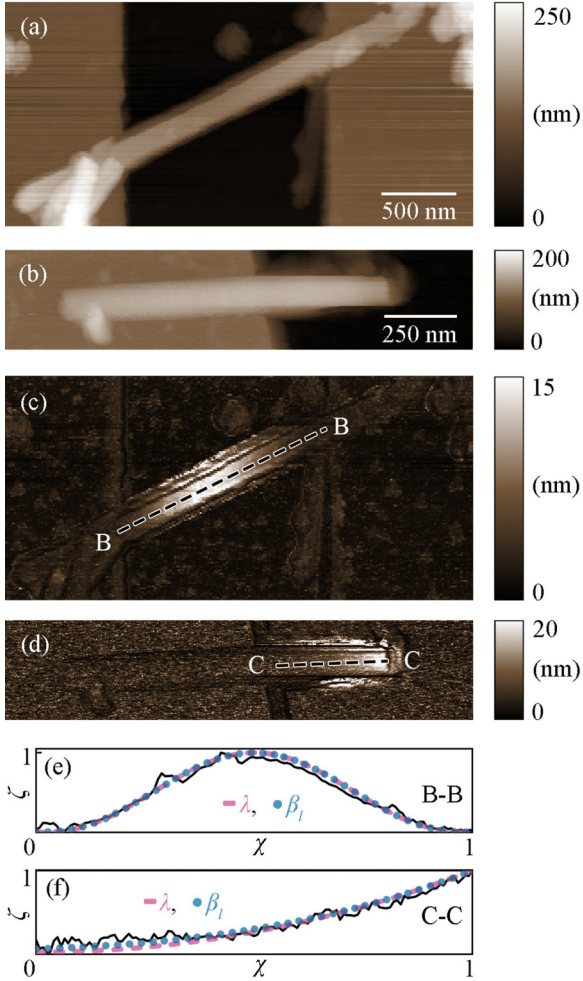


FIG. 3. AFM height images of TGZ2 grating surface with  $\text{MgNi}_2\text{Si}_2\text{O}_5(\text{OH})_4$  nanoscrolls forming (a) bridge and (b) console over a hollow in the substrate. AFM maps of corrected deformation of bridge (c) and console (d). The normalized deformation profiles  $\zeta(\chi)$  of (e) bridge and (f) console: The solid black line is the measurements, and the dashed pink and dotted blue lines are fittings according to models 1 and 2. PeakForce QNM mode parameters are as follows: The amplitude and frequency are 150 nm and 1 kHz, the scan rate and setpoint are 0.2 Hz and 30 nN (bridge) and 0.3 Hz and 25 nN (console).

that of bridges (see Table II). We also note an increase in the specific spread,  $\sigma(E)/E$ , by a factor of 2.3 (for consoles) and 1.4 (for bridges) relative to model 0. Conversely, correction by model 2 equalizes the values of  $E$  for consoles and bridges without changing  $\sigma(E)/E$ , Table II.

Applying model 2 and revealing the fixing conditions for all tested objects, one can obtain almost identical values of  $E$  for consoles and bridges. This is fully consistent with the identity of the material of the objects of both types. As a result, the combined corrected data yield the average Young’s modulus of  $E = 103 \pm 76$  GPa for  $\text{MgNi}_2\text{Si}_2\text{O}_5(\text{OH})_4$ . High standard deviation originated from individual structural features of nanoscrolls [14], whereas the accuracy of the Young’s modulus determination for each nanoscroll was below 20–25%.

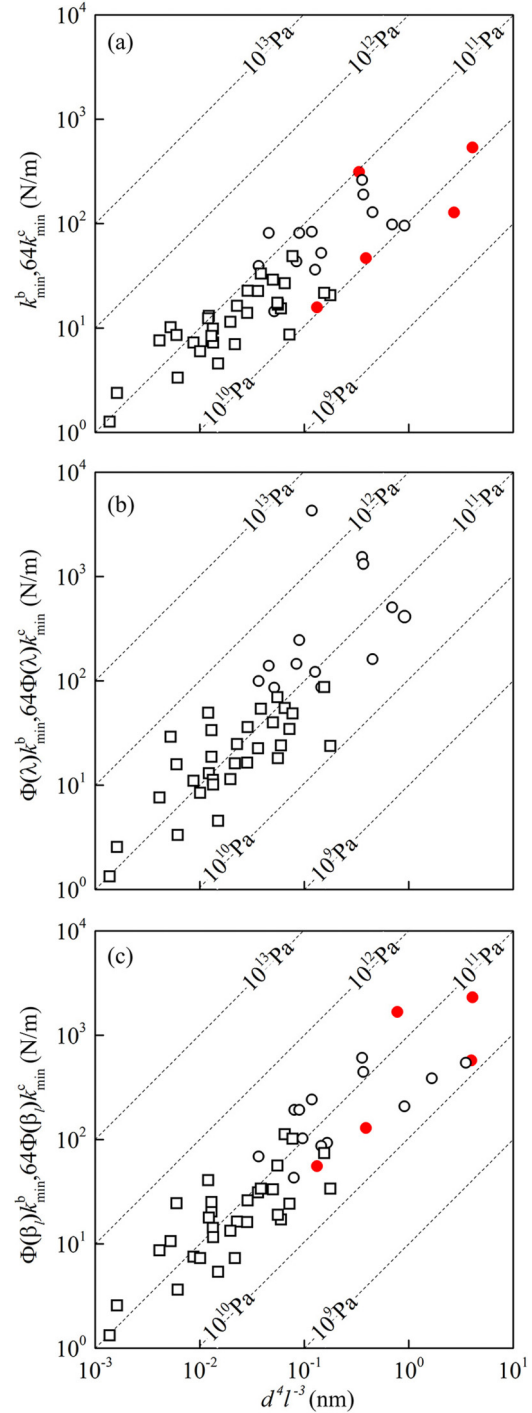


FIG. 4. Phase plane distribution of data points corresponding to bridges (squares) and consoles (circles) from  $\text{MgNi}_2\text{Si}_2\text{O}_5(\text{OH})_4$  nanoscrolls: Initial AFM data (a); corrected data using model 1 (b) and 2 (c). The  $E$  contours are shown as straight dashed lines. Due to the ability to determine the length of the suspended part of an object in two ways, the abscissas of some points corresponding to the same object on (a),(c) may not match. Filled red circles in (a) and (c) indicate data on five consoles with  $\Phi(\lambda) \rightarrow \infty$ .

The value of  $E$  calculated by the density functional theory method is approximately two times larger than the one just mentioned [14]. One can reconcile the calculation with the experiment assuming that the object deflection measured by

TABLE II. Results of calculation of the Young's modulus of  $\text{MgNi}_2\text{Si}_2\text{O}_5(\text{OH})_4$  nanoscrolls using various models.

Object type	$E \pm \sigma(E)$ (GPa)		
	Model 0	Model 1	Model 2
Bridge	$74 \pm 49$ (31)	$129 \pm 120$ (31)	$99 \pm 79$ (31)
Console	$53 \pm 48$ (18)	$481 \pm 1014$ (13)	$109 \pm 86$ (18)
Both	$66 \pm 49$ (49)	$233 \pm 569$ (44)	$103 \pm 76$ (49)

AFM consists of bending and shear deformations. Note that under this assumption, the spreads of the measured Young's and shear moduli,  $\sigma(E)$  and  $\sigma(G)$ , are also related [14]. An underrating of  $E$  by a factor of 2 corresponds to equal shear and bending deformations. According to the bridge data (see Fig. 3) one can estimate the shear modulus required for equal deflections caused by bending and shear as  $G \sim k_{\min}l/d^2 \sim 1$  GPa. Such a low value of  $G$  for layered nanotubular materials has been discussed, for example, in [6]. However, it should be added that the accuracy of measuring  $E$  decreases if the tested object has deviations in cylindricity of shape and uniformity of composition. For example, a twofold underrating of  $E$  can be due to surface contaminants, which increase the measured nanoscroll diameter by only 20%.

## V. CONCLUSIONS

An approach has been developed to analytically determine and take into account the fixing conditions in the method of AFM bending tests of suspended objects (consoles and bridges).

In the framework of the theory of small deflections of rods and disregarding shear deformations, using Krylov's functions in the asymptotic approximation, the problem about a beam partially resting on Winkler elastic foundations has been solved. A compact dependence has been obtained for the suspended beam span bending at the load point on the position of this point on the span. In addition, in the asymptotic approximation of Krylov's functions, a solution has been derived for a beam on a Winkler elastic foundation with an external console.

AFM-aided bending tests of bridges and consoles made of chrysotile hydrosilicate  $\text{MgNi}_2\text{Si}_2\text{O}_5(\text{OH})_4$  nanoscrolls were carried out. The convergence of the average values of the Young's modulus  $E$  of consoles and bridges was achieved using the developed approach for the analysis of AFM bending tests. As a result, a value of  $E = 103 \pm 76$  GPa was obtained for  $\text{MgNi}_2\text{Si}_2\text{O}_5(\text{OH})_4$ .

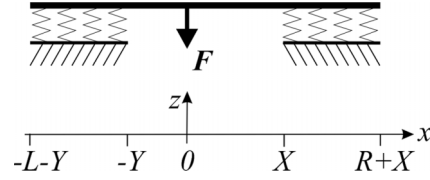


FIG. 5. Model of a beam on a Winkler elastic foundation. Beam sections from  $x = -L - Y$  to  $x = -Y$  and from  $x = X$  to  $x = R + X$  rest on elastic foundations. The middle span of length  $l = Y + X$  from  $x = -Y$  to  $x = X$  is suspended. The force  $F$  is applied at  $x = 0$ .

## ACKNOWLEDGMENT

This work was supported by the Russian Science Foundation, Project No. 19-13-00151.

## APPENDIX: CALCULATION OF A BEAM ON A WINKLER ELASTIC FOUNDATION

The deflection of the suspended span of the beam (see Fig. 5) obeys the equation  $z^{IV} = 0$  [8] with a polynomial solution of degree 3:  $z = \sum_{i=0}^3 a_i x^i$ . The side segments of the beam lie on the elastic foundation (see Fig. 5); the deflection satisfies the equation  $EIz^{IV} + k_W z = 0$  ( $E$  and  $I$  are the Young's modulus and moment of inertia of a beam of constant section, and  $k_W$  is the Winkler coefficient of the elastic foundation). The solution to this equation is a linear combination of Krylov's functions (Table III)  $z = \sum_{k=1}^4 a_k Y_k(\beta x)$ ,  $\beta = \sqrt[4]{k_W/(4EI)}$  [8,16,17]. Let us express the deflections in the four sections of the beam in general terms (see Fig. 5):

- (1) Span, length  $L$ :  $z_L = e_L Y_1[\beta(L + Y + x)] + g_L Y_2[\beta(L + Y + x)] + f_L Y_3[\beta(L + Y + x)] + h_L Y_4[\beta(L + Y + x)]$ .
- (2) Console, length  $Y$ :  $z_Y = a_Y + b_Y x + c_Y x^2 + d_Y x^3$ .
- (3) Console, length  $X$ :  $z_X = a_X + b_X x + c_X x^2 + d_X x^3$ .
- (4) Span, length  $R$ :  $z_R = e_R Y_1[\beta(R + X - x)] + g_R Y_2[\beta(R + X - x)] + f_R Y_3[\beta(R + X - x)] + h_R Y_4[\beta(R + X - x)]$ .

Unknown coefficients are sought using five boundary conditions:

- (1) At the free left end,  $x = -L - Y$ :  $z_L^{\text{II}} = z_L^{\text{III}} = 0$ .
- (2) At the free right end,  $x = R + X$ :  $z_R^{\text{II}} = z_R^{\text{III}} = 0$ .
- (3) At the load point,  $x = 0$ :  $z_Y = z_X$ ,  $z_Y^{\text{I}} = z_X^{\text{I}}$ ,  $z_Y^{\text{II}} = z_X^{\text{II}}$ ,  $z_X^{\text{III}} - z_Y^{\text{III}} = F/(EI)$ .
- (4) At  $x = -Y$ :  $z_L = z_Y$ ,  $z_L^{\text{I}} = z_Y^{\text{I}}$ ,  $z_L^{\text{II}} = z_Y^{\text{II}}$ ,  $z_L^{\text{III}} = z_Y^{\text{III}}$ .
- (5) At  $x = X$ :  $z_X = z_R$ ,  $z_X^{\text{I}} = z_R^{\text{I}}$ ,  $z_X^{\text{II}} = z_R^{\text{II}}$ ,  $z_X^{\text{III}} = z_R^{\text{III}}$ .

Applying the boundary conditions (1)–(3) and introducing the dimensionless  $x = \beta x$ ,  $L = \beta L$ ,  $R = \beta R$ ,  $\beta_l = \beta l$ ,  $X = \beta X$ , and  $Y = \beta Y$  and the coefficients  $a = a_Y = a_X$ ,  $\beta^{-1}b = b_Y = b_X$ ,  $\beta^{-2}c = c_Y = c_X$ , and  $\beta^{-3}d = d_X = d_Y + F/(6EI)$ , we write

 TABLE III. Krylov's  $Y$  functions.

$k$	$Y_k(x)$	$Y_k(0)$	$\frac{dY_k}{dx}$	$\frac{d^2Y_k}{dx^2}$	$d \frac{d^3Y_k}{dx^3}$	$Y_k(x) _{x \gg 1}$
1	$\cosh x \cos x$	1	$-4Y_4$	$-4Y_3$	$-4Y_2$	$\frac{\cosh x}{2} e^x$
2	$\frac{1}{2}(\cosh x \sin x + \sinh x \cos x)$	0	$Y_1$	$-4Y_4$	$-4Y_3$	$\frac{\sin x + \cos x}{4} e^x$
3	$\frac{1}{2} \sinh x \sin x$	0	$Y_2$	$Y_1$	$-4Y_4$	$\frac{\sin x}{4} e^x$
4	$\frac{1}{4}(\cosh x \sin x - \sinh x \cos x)$	0	$Y_3$	$Y_2$	$Y_1$	$\frac{\sin x - \cos x}{8} e^x$

(1) Span, length  $L$ :  $z_L = e_L Y_1(L + Y + x) + g_L Y_2(L + Y + x)$ .

(2) Console, length  $Y$ :  $z_Y = a + bx + cx^2 + [d - Fl^3 / (6EI\beta_l^3)]x^3$ .

(3) Console, length  $X$ :  $z_X = a + bx + cx^2 + dx^3$ .

(4) Span, length  $R$ :  $z_R = e_R Y_1(R + X - x) + g_R Y_2(R + X - x)$ .

Applying the boundary conditions (4) and (5), using the properties of the Krylov functions, Table III, after algebraic transformations, we obtain a system of equations for eight unknowns  $a, b, c, d, e_L, g_L, e_R,$  and  $g_R$ ,

$$\mathbf{M}\mathbf{v} = \mathbf{b}, \mathbf{v} = (a, b, c, d, e_L, g_L, e_R, g_R)^T,$$

$$\mathbf{b} = (0, 0, 0, 0, -Y^3, -3Y^2, -6Y, -6)^T;$$

$$\mathbf{M} = \begin{bmatrix} 1 & X & X^2 & X^3 & -Y_1(R) & -Y_2(R) & 0 & 0 \\ 0 & 1 & 2X & 3X^2 & -4Y_4(R) & Y_1(R) & 0 & 0 \\ 0 & 0 & 2 & 6X & 4Y_3(R) & 4Y_4(R) & 0 & 0 \\ 0 & 0 & 0 & 6 & -4Y_2(R) & -4Y_3(R) & 0 & 0 \\ 0 & 0 & 0 & 0 & Y_1(R) - 4Y_4(R)\beta_l - 2Y_3(R)\beta_l^2 - 2Y_2(R)\beta_l^3/3 & Y_2(R) + Y_1(R)\beta_l - 2Y_4(R)\beta_l^2 - 2Y_3(R)\beta_l^2 - 2Y_3(R)\beta_l^3/3 & -Y_1(L) & -Y_2(L) \\ 0 & 0 & 0 & 0 & -4Y_4(R) - 4Y_3(R)\beta_l - 2Y_2(R)\beta_l^2 & 4Y_1(R) - 4Y_4(R)\beta_l - 2Y_3(R)\beta_l^2 & -4Y_4(L) & Y_1(L) \\ 0 & 0 & 0 & 0 & -4Y_3(R) - 4Y_2(R)\beta_l & -4Y_4(R) - 4Y_3(R)\beta_l & 4Y_3(L) & 4Y_4(L) \\ 0 & 0 & 0 & 0 & -4Y_2(R) & -4Y_3(R) & -4Y_2(L) & -4Y_3(L) \end{bmatrix}.$$

(A1)

Solution (A1) is sought by the Cramer method. That is, the coefficient  $a$  is calculated as the ratio of determinants,  $a = |\mathbf{M}_1|/|\mathbf{M}|$ . The matrix  $\mathbf{M}_1$  is obtained by replacing column 1 in the matrix  $\mathbf{M}$  with the vector  $\mathbf{b}$ . Similarly, the vector  $\mathbf{b}$  substituted into columns 2, 3, and 4 in  $\mathbf{M}$  yields the matrices  $\mathbf{M}_2, \mathbf{M}_3,$  and  $\mathbf{M}_4$  in the calculations of  $b, c,$  and  $d$ .

Using the asymptotes of Krylov’s functions (see Table III), we obtain all coefficients of the cubic polynomial to describe the bending profile of the suspended beam span loaded with the lumped force  $F$ ,

$$a = \frac{Fl^3}{6EI\beta_l^3} \frac{3(6 + 12\beta_l + 12\beta_l^2 + 6\beta_l^3 + \beta_l^4) + 6\beta_l(3 + 4\beta_l + \beta_l^2)v + 6(1 + 3\beta_l + \beta_l^2)v^2 + 2(2 + \beta_l)v^3}{24 + 36\beta_l + 24\beta_l^2 + 8\beta_l^3 + \beta_l^4},$$

$$b = \frac{Fl^3}{2EI\beta_l^3} \frac{(1 + Y)[\beta_l^4(1 + Y) + 4\beta_l^3(Y^2 - 1) + \beta_l^2(3 - 9Y - 9Y^2 + 5Y^3) - 2\beta_l Y(3 - 6Y^2 + Y^3) + 4(Y - 1)Y^3]}{24 + 36\beta_l + 24\beta_l^2 + 8\beta_l^3 + \beta_l^4},$$

$$c = -\frac{Fl^3}{2EI\beta_l^3} \frac{2\beta_l^3(1 + Y)^2 + \beta_l^2(9 + 12Y - 4Y^3) + 2\beta_l(6 + 3Y - 6Y^2 - 4Y^3 + Y^4) + 2(3 - 3Y^2 + 2Y^4)}{24 + 36\beta_l + 24\beta_l^2 + 8\beta_l^3 + \beta_l^4},$$

$$d = \frac{Fl^3}{6EI\beta_l^3} \frac{3\beta_l^2(1 + Y)^2 + 2\beta_l(6 + 9Y + 3Y^2 - Y^3) + 4(3 + 3Y - Y^3)}{24 + 36\beta_l + 24\beta_l^2 + 8\beta_l^3 + \beta_l^4},$$

$$v = Y(\beta_l - Y). \tag{A2}$$

The bending at the load point is determined by the value of the coefficient  $a$ . It is maximum when the span midpoint is loaded,  $Y = \beta_l/2$  ( $Y = l/2$ ),

$$a_{\text{MAX}} = \frac{Fl^3}{192EI} \frac{\beta_l^3 + 24 + 12\beta_l + 6\beta_l^2}{\beta_l^3}. \tag{A3}$$

If  $\beta_l \rightarrow \infty$  ( $k_W/E \rightarrow \infty$ ), then the beam end points are clamped. In this case, we have

$$\lim_{\beta_l \rightarrow \infty} a_{\text{MAX}} = a_{\text{CB}} = \frac{Fl^3}{192E_{\text{CB}}I}. \tag{A4}$$

The ratio  $a_{\text{MAX}}/a_{\text{CB}}$  is the factor  $\Phi_2$ ,

$$\Phi_2 = 1 + 6 \frac{4 + 2\beta_l + \beta_l^2}{\beta_l^3}, \quad E_{\text{corr}} = \Phi_2 E_{\text{CB}}. \tag{A5}$$

The ratio  $a/a_{\text{MAX}}$  is the dependence  $\zeta_2$  in Table I for bridge,

$$\zeta_2 = \frac{3(6 + 12\beta_l + 12\beta_l^2 + 6\beta_l^3 + \beta_l^4) + 6\beta_l^3(3 + 4\beta_l + \beta_l^2)\chi(1 - \chi) + 6\beta_l^4(1 + 3\beta_l + \beta_l^2)\chi^2(1 - \chi)^2 + 2\beta_l^6(2 + \beta_l)\chi^3(1 - \chi)^3}{(2 + \beta_l)(12 + 12\beta_l + 6\beta_l^2 + \beta_l^3)(24 + 12\beta_l + 6\beta_l^2 + \beta_l^3)} 2^5, \tag{A6}$$

where the normalized coordinate  $\chi = Y/l$  is used, Fig. 1.

Comparing the AFM bending test data with (A6), we seek the optimum fitting parameter  $\beta_l$ ; then  $E$  is calculated from (A3)–(A5) and  $k_W$  ( $\beta_l = l\sqrt[4]{k_W/4EI}$ ).

Let us write the asymptote of the coefficient  $a$  as  $l \rightarrow \infty$  for  $\beta = \text{const}$ ,

$$\lim_{l \rightarrow \infty, \beta = \text{const}} a = \frac{F}{6EI} \frac{3 + 6Y + 6Y^2 + 2Y^3}{\beta^3}. \quad (\text{A2a})$$

Substituting  $Y = \beta_l \chi$  into (A2a), we obtain a ratio  $a/a_{\text{MAX}}$  that coincides with the dependence  $\zeta_2$  in Table I for console,

$$\zeta_2 = \frac{3 + 6\beta_l \chi + 6\beta_l^2 \chi^2 + 2\beta_l^3 \chi^3}{3 + 6\beta_l + 6\beta_l^2 + 2\beta_l^3}. \quad (\text{A6a})$$

$$\zeta_2 = \frac{3K_4(2L) + 6K_3(2L)(\beta_l \chi) + 6K_2(2L)(\beta_l \chi)^2 + 2[K_1(2L) - 1](\beta_l \chi)^3}{3K_4(2L) + 6K_3(2L)\beta_l + 6K_2(2L)\beta_l^2 + 2[K_1(2L) - 1]\beta_l^3}. \quad (\text{A6b})$$

The Krylov functions  $K_k(x)$  with the same asymptote are given in Table IV. Note that (A6b) tends to (A6a) for  $L \gg 1$ .

 TABLE IV. Krylov's  $K$  functions.

$k$	$K_k(x)$	$K_k(x) _{x \gg 1}$
1	$\frac{1}{2}(\cosh x + \cos x)$	
2	$\frac{1}{2}(\sinh x + \sin x)$	$\frac{1}{4}e^x$
3	$\frac{1}{2}(\cosh x - \cos x)$	
4	$\frac{1}{2}(\sinh x - \sin x)$	

For reference, we give the exact fitting dependence for console according to model 2 [15],

- [1] G. Binnig, C. F. Quate, and C. Gerber, Atomic Force Microscope, *Phys. Rev. Lett.* **56**, 930 (1986).
- [2] *Nanotribology and Nanomechanics. An Introduction*, edited by B. Bhushan (Springer-Verlag, Berlin-Heidelberg, 2005).
- [3] S. Magonov, M. Surtchev, J. Alexander, I. Malovichko, and S. Belikov, Mapping of nanoscale mechanical properties of polymers in quasi-static and oscillatory atomic force microscopy modes, *MRS Adv.* **1**, 2763 (2016).
- [4] J.-P. Salvétat, A. J. Kulik, J.-M. Bonard, G. A. D. Briggs, T. Stöckli, K. Méténier, S. Bonnamy, F. Béguin, N. A. Burnham, and L. Forró, Elastic modulus of ordered and disordered multiwalled carbon nanotubes, *Adv. Mater.* **11**, 161 (1999).
- [5] S. Cuenot, S. Demoustier-Champagne, and B. Nysten, Elastic Modulus of Polypyrrole Nanotubes, *Phys. Rev. Lett.* **85**, 1690 (2000).
- [6] A. Kis, Mechanical properties of mesoscopic objects, Ph.D. thesis, Ecole Polytechnique Fédérale Lausanne, EPFL, Lausanne, 2003.
- [7] D. Gangadean, D. N. McIlroy, B. E. Faulkner, and D. E. Aston, Winkler boundary conditions for three-point bending tests on 1D nanomaterials, *Nanotechnology* **21**, 225704 (2010).
- [8] L. D. Landau and E. M. Lifshitz, *Theory of Elasticity*, 2nd ed., Course of Theoretical Physics Vol. 7 (Pergamon, Oxford, 1970).
- [9] W. Mai and Z. L. Wang, Quantifying the elastic deformation behavior of bridged nanobelts, *Appl. Phys. Lett.* **89**, 073112 (2006).
- [10] Y. Chen, B. L. Dorgan, D. N. McIlroy, and D. Eric Aston, On the importance of boundary conditions on nanomechanical bending behavior and elastic modulus determination of silver nanowires, *J. Appl. Phys.* **100**, 104301 (2006).
- [11] D. Kluge, F. Abraham, S. Schmidt, H.-W. Schmidt, and A. Fery, Nanomechanical properties of supramolecular self-assembled whiskers determined by AFM force mapping, *Langmuir* **26**, 3020 (2010).
- [12] A. V. Ankudinov, A new algorithm for measuring the Young's modulus of suspended nanoobjects by the bending-based test method of atomic force microscopy, *Semiconductors* **53**, 1891 (2019).
- [13] M. Khalisov, V. Lebedev, A. Poluboyarinov, A. Garshev, E. Khrapova, A. Krasilin, and A. Ankudinov, Young's modulus of phyllosilicate nanoscrolls measured by the AFM and by the in-situ TEM indentation, *Nanosystems: Phys. Chem. Math.* **12**, 118 (2021).
- [14] A. A. Krasilin, M. M. Khalisov, E. K. Khrapova, T. S. Kunkel, D. A. Kozlov, N. M. Anuchin, A. N. Enyashin, and A. V. Ankudinov, Surface tension and shear strain contributions to the mechanical behavior of individual Mg-Ni-phyllosilicate nanoscrolls, *Part Part Syst Charact.* **38**, 2100153 (2021).
- [15] A. Ankudinov and M. Khalisov, Bending test of nanoscale consoles in atomic force microscope, *Tech. Phys. Lett.* **48**, 19 (2022).
- [16] E. Winkler, *Die Lehre von der Elastizität und Festigkeit* (Dominicus, Prague, 1867).
- [17] A. Krylov, *O raschete balok, lezhashchikh na uprugom osnovanii (in Russian)* (Akad. Nauk SSSR, Leningrad, 1931).
- [18] V. L. Popov, *Contact Mechanics and Friction: Physical Principles and Applications*, 1st ed. (Springer, Berlin-Heidelberg, 2010).
- [19] E. K. Khrapova, V. L. Ugolkov, E. A. Straumal, S. A. Lermontov, V. A. Lebedev, D. A. Kozlov, T. S. Kunkel, A. Nominé, S. Bruyere, J. Ghanbaja, T. Belmonte, and A. A. Krasilin, Front cover: Thermal behavior of Mg-Ni-phyllosilicate nanoscrolls and performance of the resulting composites in hexene-1 and acetone hydrogenation (ChemNanoMat 3/2021), *ChemNanoMat* **7**, 207 (2021).
- [20] A. A. Krasilin, E. K. Khrapova, and T. P. Maslennikova, Cation doping approach for nanotubular hydrosilicates curvature control and related applications, *Crystals* **10**, 654 (2020).
- [21] A. A. Krasilin, Energy modeling of competition between tubular and platy morphologies of chrysotile and halloysite layers, *Clays Clay Miner.* **68**, 436 (2020).
- [22] P. Scarfato, E. Avallone, L. Incarnato, and L. D. Maio, Development and evaluation of halloysite nanotube-based carrier

- for biocide activity in construction materials protection, *Appl. Clay Sci.* **132-133**, 336 (2016).
- [23] G. Cavallaro, A. Danilushkina, V. Evtugyn, G. Lazzara, S. Milioto, F. Parisi, E. Rozhina, and R. Fakhrullin, Halloysite nanotubes: Controlled access and release by smart gates, *Nanomaterials* **7**, 199 (2017).
- [24] A. A. Krasilin, D. P. Danilovich, E. B. Yudina, S. Bruyere, J. Ghanbaja, and V. K. Ivanov, Crystal violet adsorption by oppositely twisted heat-treated halloysite and pecoraite nanoscrolls, *Appl. Clay Science* **173**, 1 (2019).
- [25] C. Zhang, W. Zhu, S. Li, G. Wu, X. Ma, X. Wang, and J. Gong, Sintering-resistant Ni-based reforming catalysts obtained via the nanoconfinement effect, *Chem. Commun.* **49**, 9383 (2013).
- [26] J. Ashok, Z. Bian, Z. Wang, and S. Kawi, Ni-phyllsilicate structure derived Ni–SiO<sub>2</sub>–MgO catalysts for bi-reforming applications: Acidity, basicity and thermal stability, *Catal. Sci. Technol.* **8**, 1730 (2018).
- [27] Z. Bian and S. Kawi, Highly carbon-resistant Ni-Co/SiO<sub>2</sub> catalysts derived from phyllosilicates for dry reforming of methane, *J. CO<sub>2</sub> Util.* **18**, 345 (2017).
- [28] A. A. Krasilin, E. A. Straumal, L. L. Yurkova, E. K. Khrapova, M. V. Tomkovich, I. G. Shunina, L. P. Vasil'eva, S. A. Lermontov, and V. K. Ivanov, Sulfated halloysite nanoscrolls as superacid catalysts for oligomerization of hexene-1, *Russ. J. Appl. Chem.* **92**, 1251 (2019).
- [29] J. C. Park, S. W. Kang, J.-C. Kim, J. I. Kwon, S. Jang, G. B. Rhim, M. Kim, D. H. Chun, H.-T. Lee, H. Jung, H. Song, and J.-I. Yang, Synthesis of Co/SiO<sub>2</sub> hybrid nanocatalyst via twisted Co<sub>3</sub>Si<sub>2</sub>O<sub>5</sub>([OH])<sub>4</sub> nanosheets for high-temperature Fischer–Tropsch reaction, *Nano Res.* **10**, 1044 (2017).
- [30] Y. Liu and M. Liu, Conductive carboxylated styrene butadiene rubber composites by incorporation of polypyrrole-wrapped halloysite nanotubes, *Compos. Sci. Technol.* **143**, 56 (2017).
- [31] N. V. Afanas'eva, G. N. Gubanova, K. A. Romashkova, D. A. Sapegin, and S. V. Kononova, Relaxation processes in an aromatic polyamide-imide and composites on its basis with hydrosilicate nanoparticles, *Polym. Sci. Ser. A* **58**, 956 (2016).
- [32] H. Mo, K. Yang, S. Li, and P. Jiang, High thermal conductivity and high impact strength of epoxy nanodielectrics with functionalized halloysite nanotubes, *RSC Adv.* **6**, 69569 (2016).
- [33] K. Roy, S. C. Debnath, A. Pongwisuthiruchte, and P. Potiyaraj, Up-to-date review on the development of high performance rubber composites based on halloysite nanotube, *Appl. Clay Sci.* **183**, 105300 (2019).
- [34] J. L. Hutter and J. Bechhoefer, Calibration of atomic-force microscope tips, *Rev. Sci. Instrum.* **64**, 1868 (1993).
- [35] A. V. Ankudinov and M. M. Khalisov, Contact stiffness measurements with an atomic force microscope, *Tech. Phys.* **65**, 1866 (2020).
- [36] D. Nečas and P. Klapetek, Gwyddion: An open-source software for SPM data analysis, *Centr. Eur. J. Phys.* **10**, 181 (2012).